Molecular contacts having an orthogonal π-skeleton induce amorphization to enhance perovskite solar cell performances

Jingjing Zhou[1,2†], Yixin Luo[1†], Runda Li[1], Liuwen Tian[1,2], Ke Zhao[1,2], Jiahui Shen[1,3], Donger Jin[1], Zixuan Peng[1,3], Libing Yao[2], Li Zhang[4], Qingqing Liu[2], Shaochen Zhang[1,2], Lu Jin[1,2], Shenglong Chu[2], Sisi Wang[2], Yuan Tian[1,2], Jiazhe Xu[1,2], Xu Zhang[1,2], Pengju Shi[1,2], Xiaonan Wang[1,2], Wei Fan[1,2], Xuechun Sun[1,2], Jingyi Sun[1], Luo-zhou Chen[4], Gang Wu[5], Wen Shi[6,7], Hong-fei Wang[4], Tianqi Deng[1,8*], Rui Wang[2*], Deren Yang[1*], and Jingjing Xue[1*]

[1]State Key Laboratory of Silicon and Advanced Semiconductor Materials and School of Materials Science and Engineering, Zhejiang University, Hangzhou 310027, China

[2]School of Engineering, Westlake University and Institute of Advanced Technology, Westlake Institute for Advanced Study, Hangzhou 310030, China

[3]School of Chemistry and Chemical Engineering, Yangzhou University, Yangzhou 225002, China

[4]Department of Chemistry, Westlake University, Hangzhou, Zhejiang Province 310030, China

[5]Institute of High Performance Computing, Agency for Science, Technology and Research, 1 Fusionopolis Way, #16-16 Connexis, Singapore 138632, Singapore

[6]School of Chemistry, Sun Yat-sen University, Guangzhou, 510006, China

[7]Institute of Green Chemistry and Molecular Engineering, Sun Yat-sen University, Guangzhou, Guangdong, 510006, China

[8]Institute of Advanced Semiconductors & Zhejiang Provincial Key Laboratory of Power Semiconductor Materials and Devices, ZJU-Hangzhou Global Scientific and Technological Innovation Center, Zhejiang University, Hangzhou 311215, China

*Correspondence and requests for materials should be addressed to T.D. (email: dengtq@zju.edu.cn) or to R.W. (email: wangrui@westlake.edu.cn) or to D.Y. (email: mseyang@zju.edu.cn) or to J.X. (email: jjxue@zju.edu.cn)

[†]These authors contributed equally to this work

Abstract:

Perovskite solar cells represent a promising class of photovoltaics that have achieved exceptional performances within a short time. Such high efficiencies often depend on the use of molecule-based selective contacts that form highly ordered molecular assemblies. Although this high degree of ordering usually benefits charge carrier transport, it is disrupted by structure deformation and phase transformation upon external stresses, which limit the long-term operational stability of perovskite solar cells. Herein, we demonstrate a molecular contact having an orthogonal π-skeleton to show a superior resilience to external stimuli than the commonly used conjugated core. This molecular design yields a disordered, amorphous structure that shows a high stability while expressing exceptional charge selectivity and transport capability. The perovskite solar cells fabricated with this orthogonal π-skeleton molecule exhibited enhanced long-term durability in accelerated aging tests. This orthogonal π-skeleton functionality opens new opportunities in molecular design for applications in organic electronics.

Introduction

Molecule-based selective contact (MSC) has emerged as a pivotal component in attaining high power conversion efficiencies (PCEs) in perovskite solar cells[1-3]. The organic molecules for constructing such interlayer always consist of an oxyacid group tethered by a π-conjugation core[4-7]. When assembled at the interface between the perovskite absorption layer and the electrode, such molecular layer enabled efficient carrier selectivity and transport[8-12]. The conjugation core is essential for ensuring efficient carrier transport as it affords extended π-electron delocalization[13-14]. The extended conjugation promises ordered molecular stacking via π-π interaction, which has been widely thought to be beneficial for carrier transport in the field of organic electronics[15-18]. However, such orderly arrangement of these molecules, or described as crystallized organic structure, indicates that they always have distinct energy minima corresponding to their specific crystal structures[19-22]. This renders them susceptible to phase transformation or structure collapse when exposed to external stimuli, such as thermal and mechanical stress, which a perovskite solar cell typically encounters during practical applications[1,4,5]. Consequently, the transformed or deformed interfacial structure may lose its capability in ensuring efficient carrier transport, leading to reduction in PCEs, and ultimately limiting the long-term durability of perovskite solar cells. A solution to reconciling the structural durability and the charge carrier selectivity and transport is in urgent demand but remains a challenge.

Here, we report an orthogonal π-skeleton that produced a highly disordered structure of the as-formed molecular layer while exhibiting exceptional charge selectivity and transport capability. In contrast to the commonly used ordered or crystallized structures, the amorphous nature of this material made it free from the constraints of crystal lattice arrangements. Its homogenous energy landscape allowed it to adapt more readily to external stresses, thereby making it more resilient to various external stimuli. The perovskite solar cell fabricated with the orthogonal π-skeleton-bearing MSC exhibited

an improved PCE with considerably enhanced device durability. While the PCE of the control device with conventional ordered assembled MSC dropped to 60% of its initial PCE after ~500 h, the device with the amorphous MSC maintained over 90% over its initial PCE after tracked at maximum power point for over 2500 h at an elevated temperature of 50 ℃.

Results

Orthogonal π-skeleton induced structural disorderliness

The most commonly employed molecules for constructing the selective contacts in perovskite solar cells are based on the carbazole conjugation core, with (4-(9H-carbazol-9-yl)butyl)phosphonic acid (4PACz) as a typical example (**Fig. 1a**). By introducing a π-conjugation unit that is orthogonal to the carbazole unit, we designed and synthesized a molecule, namely (4-(10H-spiro[acridine-9,9'-xanthen]-10-yl)butyl)phosphonic acid (SAX), which features a spiro-type orthogonal π-skeleton (**Fig. 1b**, see synthesis details in Supplementary Text S1). This design resulted in a nearly perpendicular arrangement of the two molecular halves, disrupting the molecular planarity. When processed into thin films on indium tin oxide (ITO) glass substrates, 4PACz exhibited well-defined x-ray diffraction patterns centered at 5.6°, 8.6°, and 11.3°, signifying long-range orderly stacking of the molecules, whereas the film of SAX did not show any noticeable diffraction peaks (**Fig. 1c**). This indicates that the broken planarity in the conjugation core of SAX prevented it from self-stacking into crystalline structure, rendering the resulting films kind of amorphous.

The analysis of the films using polarization-dependent Raman spectroscopy in **Fig. 1d** revealed that the intensity of the Raman peak at ~1600 cm^{-1} stemming from the stretching of aromatic C=C bonds in 4PACz varied significantly with the polarized angle. This variation underscores the structural anisotropy, a characteristic of crystalline structures that feature directional molecular packing. In contrast, the peak intensity corresponding to the C=C stretching in the orthogonal π-skeleton of the SAX film was almost independent of the polarized angle **(Fig. 1e)**. This observation, consistent with the XRD results, indicates a relatively random arrangement of molecular skeleton, devoid of long-range orderliness, thereby imparting structural isotropy to the film. Sub-1 cm^{-1} High Resolution Broadband Sum Frequency Generation Vibrational Spectroscopy (HR-BB-SFG-VS), which selectively probes the vibrational spectra of the interfacial molecular layer[23], was used to study the molecular packing at the glass interface (see experimental details in Supplementary Text S2). The SFG-VS signal shown in **Fig. 1f** is an average over the spectra obtained from 10 different sites in each sample, with an exposure of 1000 s in each measurement to gain higher reliability and signal-to-noise ratio of the SFG-VS data. 4PACz exhibited an evident SFG-VS peak centered at 3050 cm^{-1}, corresponding to the aromatic C-H stretching mode in the conjugation unit (Supplementary Fig. 1-2), which indicates a highly ordered self-assembled monolayer at the interface (Supplementary Text S2). In comparison, the SFG-VS signal in the SAX sample significantly dropped, suggesting a substantial reduction in the orderliness of the interfacial molecular packing. These results confirm that the orthogonal π-skeleton impeded the ordered stacking and,

consequently, the crystallization of the molecules, leading to a highly disordered amorphous phase as schematically depicted in **Fig. 1g and Fig. 1h**.

Enhanced resistance to external stimuli

We evaluated the structural stability of the 4PACz and SAX thin films under different external stimuli via atomic force microscopy (AFM). The evolution of the surface microstructure of the molecular films before and after continuous heating at 65 ℃ is displayed in **Fig. 2a**. After an aging course of 400 h, the 4PACz exhibited evident aggregation, whereas the SAX film remained almost unchanged, maintaining a homogenous surface landscape. We varied the aging temperature to cross-verify the results, and similar trends were observed for the test at 100 ℃ (Supplementary Fig. 3). We also tested their resistance to mechanical stress by depositing the molecular films onto polyethylene terephthalate flexible substrates, and imposed cyclic stretching stress on the films. After 50 cycles of stretching, the 4PACz film showed large block- or string-like features, indicating that the initial molecular stacking of 4PACz was significantly affected upon mechanical stress (**Fig. 2b**). In contrast, the SAX film remained its initial surface features due to the lack of ordering in the molecular packing, which enabled the molecules to adapt more readily when subjected to stress. The random vacant spaces within the film can also allow the material to adsorb and dissipate energy more effectively during loading, making it resilient to external stress.

We utilized Molecular dynamics (MD) simulations to gain further insights into the configurational evolution of the molecular packing under external stimuli (see supplementary Text S3 for computational details). As shown in **Fig. 2c**, the 4PACz molecular cluster tends to aggregate after annealing, with the initial π-π stacking of the carbazole conjugation core disrupted. For the SAX molecular cluster, despite changes in the relative position of each molecule after annealing, its molecular packing mode of high disorders remained almost unchanged, exhibiting high ensemble homogeneity (**Fig. 2d)**. These theoretical results align well with the experimental XRD results, which presents the evolution in the diffraction patterns of these films upon annealing. During the annealing process, the intensity of the diffraction peaks of the 4PACz film gradually decreased with evident peak broadening, suggesting reduced crystallinity and disrupted molecular stacking. For extended aging duration, a shift in the peak positions was detected, pointing towards potential phase transformation or an expansion of the molecular lattice structure (**Fig. 2e**). In contrast, throughout the aging period, the SAX film consistently displayed no discernible diffraction peaks, indicating that it remained amorphous and microstructurally disordered (**Fig. 2f**). We also utilized SFG-VS to monitor the structural evolution of the molecular interface during elongated exposure to laser beam (Supplementary Fig. 4). In the 4PACz film, the SFG-VS signal stemming from the aromatic C-H bond gradually weakened as the duration of light exposure increased, signifying a disruption in the stacking pattern between the conjugation cores at the interface. Conversely, the SFG-VS signal of the SAX film remained consistently low throughout the light exposure, complementing the XRD findings and highlighting the persistent structural disorder within the SAX film.

We performed conductive-AFM measurements to assess the electronic properties of the as-fabricated molecular films. These measurements synchronized with the AFM results, ensuring data collection from identical locations and timeframes. Both 4PACz (**Fig. 3a**) and SAX (**Fig. 3b**) delivered homogeneous surface electronic properties of the freshly prepared films, yet SAX stands out with a higher average surface current signal of approximately 3.8 nA compared to 0.7 nA of 4PACz. The elevated conductivity suggests superior charge transport capabilities of the SAX film (see Supplementary Text S3 for the analysis of the conductivity difference in 4PACz and SAX), thereby proving it as a promising MSC material despite its lack of long-range ordering of molecular stacking. Upon heating, the surface current signal of the 4PACz film dramatically dropped, whereas the signal of the SAX film retained at a high level. A similar trend in the change of the current signal was also observed when mechanical stresses were applied on these films (**Fig. 3c and Fig 3d**). The bar charts illustrate the statistical results of the current signals collected from different samples, affirming the notable reduction in conductivity of the aged 4PACz films, in sharp contrast to the nearly unaffected charge transport capability in SAX samples. We extended our thermal stability assessments to more control molecules, including the most widely used 2PACz, MeO-2PACz, Me-4PACz. XRD measurements unveiled a gradual decline in diffraction peak intensities during aging of all these molecular films, accompanied with peak broadening and peak shift, indicative of disrupted molecular stacking (Supplementary Fig. 5). Molecular aggregation, albeit to a lesser extent compared to 4PACz, was also observed in the AFM results obtained in these films. Due to the changed molecular stacking configuration, the conductivity of the film decreased as signified by the drop in the surface current signal measured by the conductive-AFM (Supplementary Fig. 6).

We attribute the decline in the conductivity to the deformed molecular stacking and aggregation. This can be evidenced by the observation that lower c-AFM signals were consistently recorded in regions with convex landscapes when analyzed using AFM (Supplementary Fig. 7). Based on the MD simulation results noted earlier, we modeled the charge transport dynamics in these molecular films before and after the annealing process based on a charge-hopping mechanism described by the Marcus theory. The charge mobility in the initial molecular cluster was calculated to be 0.26 and 0.93 cm^2 V^{-1} s^{-1} for 4PACz and SAX respectively (Supplementary Text 3). The higher calculated mobility in the SAX is consistent with the higher surface current signal as revealed by the c-AFM measurement. Although the mobility in the case of the SAX was higher than that of the 4PACz, they were in general on the same order of magnitude, sufficient to ensure charge transport at the interface. However, upon annealing, the mobility of the 4PACz underwent a substantial drop to 0.005 cm^2 V^{-1} s^{-1}, two orders of magnitude lower than its initial value, whereas the mobility of the SAX remained relatively stable, maintaining a similar order of magnitude as its initial state. **Fig. 3e** shows a schematic illustration of the underlying mechanism of the superior stability in terms of the charge transport capability in the amorphous SAX film than the crystalline 4PACz film. For the crystalline 4PACz film, it features ordered molecular stacking and specific crystal structure, which provides a specific network or crystallographic plane for optimal

charge transport pathway. However, this ordered structure also makes them more susceptible to phase deformation when exposed to external stimuli. Since the charge carriers rely on the specific crystalline pathways for efficient transport, any disruption to these pathways can significantly reduce the overall conductivity of the film. In contrast, the highly disordered molecular arrangement in the amorphous SAX films leads to a more uniform distribution of structural defects, which allows for charge transport to occur with less reliance on specific crystalline pathways. Therefore, even when exposed to external factors that might alter the local structure, the overall conductivity of the film is less likely to be greatly impacted.

We conducted the ultraviolet photoelectron spectroscopy (UPS) measurements to assess the band characteristics of the assembled MSCs. The obtained UPS spectra and corresponding extracted band diagrams extracted for the SAX and 4PACz samples are compared in **Fig. 3f and Fig. 3g**. Both the 4PACz and SAX films exhibited a similar UPS cut-off energy at ~16.2 eV, indicating their comparable Fermi levels. However, a distinction was observed in the UPS onset, with the SAX film showing a value of 0.47 eV, while the 4PACz exhibiting a higher value of 0.78 eV (**Fig. 3h**). This indicates that the MSC derived from SAX possesses a more pronounced p-type characteristic, which could potentially promote the hole selectivity and transport across the interface. We further evaluated the changes in the energy levels of the films before and after mechanical stretching. The UPS cut-off and on-set for 4PACz shifted evidently, suggesting altered molecular stacking that significantly changed the Fermi level and the valence band maximum of the films. In contrast, neither the UPS cut-off nor on-set showed noticeable shifts in the SAX sample after stretching, suggesting that the energy levels of film were not affected (Supplementary Fig. 8). These results in combination with the conductive-AFM results noted earlier, demonstrate the superiority of the amorphous structure in stabilizing the electronic properties. We also used Kelvin probe force microscopy to investigate the surface potential distribution of the molecular films. As shown in Supplementary Fig. 9, the SAX film generally showed a slightly higher surface potential than that of the 4PACz, which was consistent with the UPS results. The SAX film exhibits a more homogeneous distribution of surface potential compared to the 4PACz film. This homogeneity could be attributed to its highly disordered microstructure, lacking distinct crystalline domains that could potentially impart variations in local surface potential.

We further extended our investigations to a series of molecules featuring different π-orthogonal skeletons (Supplementary Text S4). The results demonstrate that the structural design of orthogonal π-skeletons serve as a universal strategy to induce structural amorphousness which can deliver superior resistance to external stimuli and thus stabilize the electronic properties of the films. By delving deeper into the intricate structure-property interplay of this molecular family, we also formulated more comprehensive design principles particularly in terms of rational modulation of the electronic properties, providing guidelines for device fabrications.

Photovoltaic performances

We evaluated the photovoltaic performances of the perovskite solar cell devices fabricated using SAX as the MSCs, with 4PACz investigated in parallel for comparison. The solar cells were fabricated with an inverted device architecture of ITO/4PACz or SAX/$Cs_{0.05}(FA_{0.98}MA_{0.02})_{0.95}Pb(I_{0.98}Br_{0.02})_3$/LiF/$C_{60}$/BCP/Ag. The best-performing device with 4PACz showed a PCE of 22.4%, with an open-circuit voltage (V_{OC}) of 1.14 V, a short-circuit current (J_{SC}) of 25.2 mA cm^{-2}, and a fill factor (FF) of 78.1% (**Fig. 4a**). Upon replacing the 4PACz with the SAX, the champion device yielded a considerably improved PCE up to 25.1% at a reverse scan with a stabilized PCE of 24.8% (Supplementary Fig. 10). The champion device exhibited a V_{OC} of 1.17 V, a J_{SC} of 25.7 mA cm^{-2}, and a FF of 83.4%. The statistical photovoltaic parameters are presented in Supplementary Fig. 11, which confirmed good reproducibility of the PCE improvement with SAX (18% improvement in an average PCE from 20.8 ± 2.4% to 24.5 ± 0.6%). As the enhancement in PCE primarily arose from the increased FF, we extracted the shunt resistance R_{sh} and series resistance R_s of the devices to better understand the improvement. The R_{sh} value for 4PACz and SAX was determined to be 2875.14 Ω and 4758.48 Ω, respectively. The increased R_{sh} in SAX-based device suggests lower current leakage than that in 4PACz-based device. This can be attributed to the greater freedom and flexibility of the molecular stacking of SAX, which could lead to the formation of a denser interlayer preventing the perovskite from directly contacting ITO. The R_s value for 4PACz and SAX was determined to be 31.29 Ω and 23.92 Ω, respectively. The decrease in R_s indicates a lower interfacial resistance in SAX, which aligned well with the higher conductivity as revealed by the c-AFM results presented earlier.

To gain further mechanistic insights into the PCE improvement, we measured the time-resolved photoluminescence (TRPL) of the perovskite films in contact with the molecular films under different laser power intensities and derived the differential lifetime to delineate the interfacial carrier dynamics. The differential lifetime can show two clearly distinguishable time intervals at a relatively low laser fluence. The first interval at short times is dominated by the charge transfer, and the second interval at longer times is governed by carrier recombination (**Fig. 4b**). For higher laser fluences the two lifetimes are less easy to distinguish due to stronger charge accumulation at the interface (Supplementary Fig. 12). At both relatively low and higher laser fluence, the first intervals for SAX were shorter than those of 4PACz, verifying improved charge extraction in SAX compared to 4PACz. For a relatively high laser fluence, the two lifetimes resulting charge transfer and recombination are less distinguishable in 4PACz than SAX, which might also indicate less charge accumulation at the interface for SAX[24,25]. Moreover, we performed the transient photocurrent decay (TPC) measurements for the SAX and 4PACz-based devices (**Fig. 4c**). The SAX-based device demonstrated a faster TPC decay profile than that of the 4PACz-based device, which further corroborates the facilitated hole extraction at the interface[3].

We extended the application of SAX to various fabrication scenarios of perovskite devices to demonstrate its universal effectiveness. We tested it in the solar cell device with a wide bandgap perovskite absorber ($Cs_{0.05}MA_{0.15}FA_{0.8}PbI_{2.25}Br_{0.75}$). The wide bandgap cells were sub-cells of critical importance for tandem devices. The current

density-voltage (*J-V*) curves of the best-performing wide bandgap devices based on 4PACz and SAX are compared in **Fig. 4d**. While the 4PACz-based device showed a PCE of only 21.5%, the SAX-based device yielded a champion PCE of 23.0%, which was among the highest PCE for wide band gap perovskite solar cells. The statistical photovoltaic parameters obtained from 12 devices for each condition is shown in Supplementary Fig. 13, demonstrating an average PCE of 20.9% and 22.8% for 4PACz and SAX, respectively.

We also fabricated the solar cells on flexible substrates to evaluated the resistance of the devices to mechanical stresses. We obtained a PCE of 23.4% and 21.0% for SAX and 4PACz based flexible devices respectively (Supplementary Fig. 14). After mechanical stretching, we observed that the *J-V* performance of the SAX based device showed negligible degradation. In contrast, the 4PACz based device exhibited evident reduction in the PCE from 21.0% to only 15.9%, primarily stemming from the decrease in the J_{sc} (from 25.1 to 22.4 mA/cm^2) and FF (from 73.2% to 62.1%). The decreased J_{sc} along with the increased series resistance could be attributed to the reduced charge extraction and transport capability at the interface. We conducted time-resolved photoluminescence (TRPL) measurements to study the carrier dynamics at the interface between the molecular layers and the perovskite layers. As shown in Supplementary Fig. 15, the first interval for SAX was shorter than that of 4PACz, indicating better charge extraction in SAX compared to 4PACz. After stretching, the first interval of SAX along with its overall TRPL profile remained almost unchanged, whereas the first interval of 4PACz increased, suggesting compromised charge extraction capability of the 4PACz layer after stretching. We also measured the TPC of the devices before and after the mechanical stretching as displayed in Supplementary Fig. 16. The TPC of the SAX based device showed a faster decay profile, which remained almost unchanged after stretching. In contrast, the TPC of the 4PACz based device became significantly slower after stretching, verifying the worse charge extraction capability of 4PACz upon mechanical stress.

We tracked the changes in PCEs of the perovskite cells under accelerated-aging conditions according to the International Summit on Organic Photovoltaic Stability (ISOS) protocols to evaluate the longevity of the devices. To address the intrinsic thermal stability, we followed the ISOS-D-2 protocol to age the devices in the dark at 85 ℃. While the PCE of the control device dropped to 50% of its initial PCE, the device based on SAX retained over 95% of its initial PCE after 1000 h, justifying the superiority of SAX to 4PACz in resistance to heat (Supplementary Fig. 17). Following the ISOS-L-2 protocol, the devices were aged under continuous one-sun illumination at 65 ℃. Compared to the swiftly dropped PCE of the 4PACz-based device, the SAX-based device retained over 97% of its initial PCE after 2000 h (**Fig. 4e**). We also tracked the PCE evolution under maximum power point, with a testing temperature of ~50 ℃. The SAX-incorporated device showed much slowed decay in PCE than its 4PACz counterpart, retaining over 91.5% of its maximum PCE after ~2500 h (**Fig. 4f**). MPP tracking at an even higher temperature of 85 ℃ was also performed. The PCE of the control device swiftly dropped to 70% of its initial PCE after 65 h, whereas the device based on SAX retained ~90% of its initial PCE after 400 h (Supplementary Fig. 18).

These results demonstrate that the improved resistance of MSC to external stimuli can strengthen the interface between the perovskite layer and the electrode, thus significantly suppressing the degradation of perovskite devices and elongating their operational lifetimes.

Discussion

While all MSCs reported so far for high-efficiency perovskite solar cells are limited to conjugation moieties characterized by strong molecular packing and crystallization capabilities, we developed a distinct conjugation core delivering an amorphous structure. This highly disordered structure, attributed to its greater flexibility in molecular arrangement and charge transport pathways, exhibited enhanced resilience to external stimuli compared to its crystalline counterparts. The as-fabricated perovskite solar cell devices demonstrated improvements in both the PCE and operational stability. Our unique π-skeleton design to render amorphousness without compromising its electronic properties may open up more opportunities in molecular design for such purpose, and inspire future research to unlock the full potential of this molecular family for organic electronics.

Acknowledgements:

All the authors thank L. Liu, Y. Nie and T. Zhou from Instrumentation and Service Center for Physical Sciences (ISCPS), X. Lu, Y. Chen, Z. Chen, Y. Cheng, D. Gu, C. Wang and M. Zhou from Instrumentation and Service Center for Molecular Sciences at Westlake University for the assistance in the characterizations. J.Xue. acknowledges the grant by the National Natural Science Foundation of China (Grant No. 62274146). J. Xue and R.W. acknowledge grants (grant numbers LR24F040001, LD22E020002 and LD24E020001) from the Natural Science Foundation of Zhejiang Province of China. J.Xue. acknowledges the grant by the financial support by Shanxi-Zheda Institute of Advanced Materials and Chemical Engineering (2021SZ-FR006), and the support by the Foundation for Innovative Research Groups of the National Natural Science Foundation of China (Grant No. 61721005). R.W. acknowledges the grant by National Natural Science Foundation of China (Grant No. 62474143) and the support of Key R&D Program of Zhejiang (2024SSYS0061) This work was also supported by the National Natural Science Foundation of China (Grant No. 62204209), the Fundamental Research Funds for the Central Universities (226-2022-00200), and Muyuan Laboratory (Program ID: 14136022401). H.F.W. acknowledges the National Key Instrumentation Development grant by the National Natural Science Foundation of China (Grant No. 21727802).

Author Contributions Statement:

J.Xue, R.W., J.Z. and Y.L. conceived the idea. J.Z. synthesized all molecules. J.Z., R.L. and L.T. did the fabrication of perovskite films and devices. J.Z. and Y.L. did the data analysis under the supervision of R.W. and J.Xue. K.Z., J.Shen, D.J., Z.P., L.Y., Q.L., S.Z., L.J., S.C., S.W., Y.T., J.Xu., X.Z., P.S., X.W., W.F., P.S., X.S. and J.Sun. assisted with the characterizations and device fabrication. L.Z. and L.Z.C. conducted the SFG-VS experiment with J.Z. under the supervision of H.F.W. G.W., W.S. and T.D.

conducted the theoretical calculations. D.Y. provided insightful discussions. J.Xue wrote the manuscript. All the authors discussed the results and commented on the manuscript.

Competing Interests Statement:

The authors declare no competing interests.

Figure Legends:

Fig. 1 Molecular design and stacking behavior. a,b, Molecular structures of 4PACz (a) and SAX (b). **c**, XRD patterns of assembled 4PACz and SAX films. **d,e**, Polarization-dependent Raman spectroscopy of the 4PACz (d) and SAX (e) films. **f**, SFG-VS of the 4PACz and SAX films. **g,h**, Schematics of the molecular assembly of the 4PACz (g) and SAX (h).

Fig. 2 Amorphization induced structural stability. Surface microstructures of the 4PACz and SAX films before and after **a**, thermal stress and **b**, mechanical stress. **c**,**d**, Molecular dynamics simulations of the molecular arrangement of 4PACz (c) and SAX (d) before and after annealing. **e**,**f,** Evolution of the XRD patterns of the 4PACz (e) and SAX (f) films upon annealing.

Fig. 3 Electronic properties of the molecular films. a,b, Conductive-AFM images and the statistical results of the spatially averaging surface current signals of the 4PACz (a) and SAX (b) films before and after thermal stress. Data are presented as mean value ± s.d. Sample size n is defined as the number of films measured by conductive-AFM: n=3 for all cases. **c,d**, Conductive-AFM images and the statistical results of the spatially averaging surface current signals of the 4PACz (c) and SAX (d) films before and after mechanical stress. Data are presented as mean value ± s.d. Sample size n is defined as the number of films measured by conductive-AFM: n=3 for all cases. **e**, Schematics of the evolution in the molecular stacking and the carrier transport pathways in the 4PACz and SAX films under external stimuli. **f,g**, UPS results of the 4PACz (f) and SAX (g) films. **h**, The derived band diagrams of the 4PACz and SAX films.

Fig. 4 Photovoltaic performances. a, *J-V* curves of best-performing solar cells with narrow bandgap perovskite employing 4PACz and SAX as the MSCs respectively. **b**, Differential lifetime $\tau_{PL}(t)$ derived from TRPL measurements at a low laser fluence of 2.6 nJ/cm^2 for perovskite films in contact with 4PACz and SAX. **c**, Comparison of the TPC results of the 4PACz and SAX based solar cell devices. **d**, *J-V* curves of best-performing solar cells with wide bandgap perovskite employing 4PACz and SAX as the MSCs respectively. **e**, Evolution of the PCEs tracked at open-circuit condition under continuous one-sun illumination and thermal stress of ~65 ℃ following the ISOS-L-2 protocol. Data are presented as mean value ± s.d. Sample size n is defined as the number of devices tested: n=3 for 4PACz and n=4 for SAX. **f**, Maximum power point tracking of the perovskite solar cells under continuous one-sun light illumination at ~ 50 ℃ for 4PACz and SAX.

References:

1. Jiang, Q. & Zhu, K. Rapid advances enabling high-performance inverted perovskite solar cells.

Nat. Rev. Mater. **9**, 399-419 (2024).
2. Zhang, S. et al. Minimizing buried interfacial defects for efficient inverted perovskite solar cells. *Science* **380**, 404-409 (2023).
3. Zhu, J. et al. A donor–acceptor-type hole-selective contact reducing non-radiative recombination losses in both subcells towards efficient all-perovskite tandems. *Nat. Energy* **8**, 714-724 (2023).
4. Yu, S. et al. Homogenized NiOx nanoparticles for improved hole transport in inverted perovskite solar cells. *Science* **382**, 1399-1404 (2023).
5. Jiang, Q. et al. Towards linking lab and field lifetimes of perovskite solar cells. *Nature* **623**, 313-318 (2023).
6. Zhang, H. et al. Formamidinium Lead Iodide-Based Inverted Perovskite Solar Cells with Efficiency over 25 % Enabled by An Amphiphilic Molecular Hole-Transporter. *Angew. Chem. Int. Ed.* **63**, e202401260 (2024).
7. Li, L. et al. Flexible all-perovskite tandem solar cells approaching 25% efficiency with molecule-bridged hole-selective contact. *Nat. Energy* **7**, 708-717 (2022).
8. He, R. et al. All-perovskite tandem 1 cm^2 cells with improved interface quality. *Nature* **618**, 80-86 (2023).
9. Wu, T. et al. Graphene-Like Conjugated Molecule as Hole-Selective Contact for Operationally Stable Inverted Perovskite Solar Cells and Modules. *Adv. Mater.* **35**, 2300169 (2023).
10. Zhang, S. et al. Conjugated Self-Assembled Monolayer as Stable Hole-Selective Contact for Inverted Perovskite Solar Cells. *ACS Materials Lett.* **4**, 1976-1983 (2022).
11. Ge, Q. Q. et al. A Two-Dimensional Hole-Transporting Material for High-Performance Perovskite Solar Cells with 20 % Average Efficiency. *Angew. Chem. Int. Ed.* **57**, 10959-10965 (2018).
12. Guo, H. et al. A Coplanar π-Extended Quinoxaline Based Hole-Transporting Material Enabling over 21 % Efficiency for Dopant-Free Perovskite Solar Cells. *Angew. Chem. Int. Ed.* **60**, 2674-2679 (2020).
13. Gao, Y. et al. Highly Stable Lead-Free Perovskite Field-Effect Transistors Incorporating Linear π-Conjugated Organic Ligands. *J. Am. Chem. Soc.* **141**, 15577-15585 (2019).
14. Dou, L., Liu, Y., Hong, Z., Li, G. & Yang, Y. Low-Bandgap Near-IR Conjugated Polymers/Molecules for Organic Electronics. *Chem. Rev.* **115**, 12633-12665 (2015).
15. Li, G., Chang, W.-H. & Yang, Y. Low-bandgap conjugated polymers enabling solution-processable tandem solar cells. *Nat. Rev. Mater.* **2**, 17043 (2017).
16. Sun, G. et al. High performance polymerized small molecule acceptor by synergistic optimization on π-bridge linker and side chain. *Nat. Commun.* **13**, 5267 (2022).
17. Meng, D. et al. Configurable Organic Charge Carriers toward Stable Perovskite Photovoltaics. *Chem. Rev.* **122**, 14954-14986 (2022).
18. Ma, K. et al. Multifunctional Conjugated Ligand Engineering for Stable and Efficient Perovskite Solar Cells. *Adv. Mater.* **33**, 2100791 (2021).
19. Ma, R. et al. Unveiling the Morphological and Physical Mechanism of Burn-in Loss Alleviation by Ternary Matrix Toward Stable and Efficient All-Polymer Solar Cells. *Adv. Mater.* **35**, 2212275 (2023).
20. Hu, H. et al. Synergistic strategy of rigid-bridge and flexible-bridge achieving high-performance and mechanical robustness all-Polymer solar cells. *Chem. Eng. J.* **491**, 152009

(2024).
21. Yi, J., Zhang, G., Yu, H. & Yan, H. Advantages, challenges and molecular design of different material types used in organic solar cells. *Nat. Rev. Mater.* **9,** 46-62 (2023).
22. Fu, J. et al. Rational molecular and device design enables organic solar cells approaching 20% efficiency. *Nat. Commun.* **15,** 1830 (2024).
23. Wang, H. F., Velarde, L., Gan, W. & Fu, L. Quantitative Sum-Frequency Generation Vibrational Spectroscopy of Molecular Surfaces and Interfaces: Lineshape, Polarization, and Orientation. *Annu. Rev. Phys. Chem.* **66,** 189-216 (2015).
24. Krogmeier, B., Staub, F., Grabowski, D., Rau, U. & Kirchartz, T. Quantitative analysis of the transient photoluminescence of CH3NH3PbI3/PC61BM heterojunctions by numerical simulations. *Sustain. Energy & Fuels* **2**, 1027-1034 (2018).
25. Krückemeier, L., Krogmeier, B., Liu, Z., Rau, U. & Kirchartz, T. Understanding Transient Photoluminescence in Halide Perovskite Layer Stacks and Solar Cells. *Adv. Energy Mater*. **11**, 2003489 (2021).

Methods:

Materials

All materials used in this work were obtained commercially and used without further purification unless otherwise specified. The transparent ITO glass substrates (ITO, 10 Ω per square, transmittance 88%) was purchased from Shenzhen Huayu United Technology Co., Ltd. The perovskite raw materials including lead iodide (PbI_2, purity 99.999%, perovskite grade), methylammonium bromide (MABr, purity 99.9%), formamidinium iodide (FAI, purity 99.99%), methylammonium chloride (MACl, purity 99.9%), lithium fluoride (LiF, purity 99.99%) and C_{60} (purity 99.9%) were all purchased from Advanced Election Technology Co., Ltd. Bathocuproine (BCP, purity 99%), cesium iodide (CsI, purity 99.999%), oleylammonium iodide (OAmI, purity 99.5%) and (4-(9H-carbazol-9-yl)butyl)phosphonic acid (4PACz, purity 99%) were purchased from Xi'an Polymer Light Technology Corp. Inc. The required solvent including *N*, *N*-Dimethylformamide (DMF, extra dry, purity 99.8%), dimethyl sulfoxide (DMSO, anhydrous, ≥99.9%), isopropanol (IPA, extra dry, purity 99.5%), methanol (extra dry, purity 99.8%) and chlorobenzene (CB, e anhydrous, ≥99.9%), ethyl acetate (EA, extra dry, purity 99.5%) and silver (Ag, purity 99.99%) were purchased from Sigma-Aldrich Inc. The following compounds: 10H-spiro[acridine-9,9'-xanthene], 10H-spiro[acridine-9,9'-thioxanthene], 10H,10'H-spiro [acridine-9,9'-anthracen]-10'-one, 2,7-dimethyl-10H-spiro [acridine-9,9'-fluorene], 10H-spiro [acridine-9,9'-fluorene], 2,7-dibromo-10H-spiro [acridine-9,9'-fluorene], 2',7'-dibromo-10H-spiro [acridine-9,9'-fluorene] were all purchased from Zhengzhou Alfa Chemical Co., Ltd. Triethylsilane (99%), bromotrimethylsilane (TMSBr, 98%), Chloroform-*d* ($CDCl_3$, 99.8%) and dimethyl sulfoxide-d_6 (DMSO-d_6, 99%) were purchased from J&K Scientific. 1,4-dibromobutane, tetrabutylammonium bromide, triethyl phosphite (98%), methanol (99.7%), dioxane (99.7%, SafeDry, with molecular sieves) were purchased from Innochem. Potassium hydroxide (KOH, 85%) was purchased from Greagent.

Perovskite precursor and film preparation

For the preparation of narrow bandgap perovskite films with a composition $Cs_{0.05}(FA_{0.98}MA_{0.02})_{0.95}Pb(I_{0.98}Br_{0.02})_3$, 1.65 M perovskite precursor solution was prepared by dissolving CsI, MABr, FAI, $PbBr_2$ and PbI_2 in mixed solvent of DMF and DMSO at volume ratio 4:1. Additional 7 mol% PbI_2 and 15 mol% MACl was added to the precursor solution and the solution was stirred overnight. Then the filtered perovskite precursor was spin-coated on substrate at 1000 rpm for 6 s and 5000 rpm for 40 s in nitrogen glovebox. 250 μL of CB as anti-solvent was dripped onto the substrate quickly at 23-25 s during the second spinning step. Afterwards, the perovskite film was annealed at 110 °C for 20 min.

For the preparation of wide bandgap perovskite films with a composition $Cs_{0.05}FA_{0.8}MA_{0.15}Pb(I_{0.75}Br_{0.25})_3$, 1.40 M perovskite precursor solution was prepared by dissolving CsI, FAI, MABr, $PbBr_2$ and PbI_2 in mixed solvent of DMF and DMSO at volume ratio 4:1. Additional 5 mol% PbI_2 and 10 mol% MACl was added to the precursor solution and the solution was stirred overnight. Then the filtered perovskite precursor was then spin-coated on substrate at 1000 rpm for 10 s and 5000 rpm for 40 s in nitrogen glovebox. 200 μL of EA as anti-solvent was dripped quickly at 20-18 s during the second spinning step. Afterwards, the film was annealed at 110 °C for 30 min.

Fabrication of inverted PSCs devices

Firstly, the pre-patterned ITO glass substrates (15 mm × 15 mm) were washed consecutively with detergent solution, deionized water, acetone, and isopropanol (IPA), each under 30 min of sonication, followed by drying with a pure nitrogen flow. The cleaned and dried ITO glass substrates were then treated with ultraviolet-ozone for 35 min, and then transferred into glovebox filled with nitrogen. To deposit 4PACz or SAX layer on ITO glass substrates, the filtered 4PACz or SAX solution with 0.002 mmol/mL in mixed solvent of methanol and DMF at volume ratio 2:1 was spin-coated at 1000 rpm for 10 s and 3000 rpm for 40 s in nitrogen glovebox. Afterwards, the film was annealed at 130 ℃ for 20 min. After cooling down to room-temperature, perovskite films were coated on 4PACz or SAX layer following the previously mentioned method. The previously noted spin-coating processes were all conducted at room temperature (20–23 ℃) in nitrogen. For the surface passivation layer, the OAmI was dissolved in IPA with a concentration of 1.0 mg mL^{-1} and stirred at room temperature (20–25 ℃) for 2 h. 60 μL of OAmI solution was spin-coated on top of the as-prepared perovskite at 5000 rpm for 40 s, and then transferred to the hotplate and annealed at 100 ℃ for 1 min.

After cooling down to room-temperature, the whole device was transferred to a vacuum chamber under a base pressure of $<5.0\times10^{-6}$ Pa. 0.7 nm LiF at a rate of 0.1 Å s^{-1}, 30 nm C_{60} at a rate of 0.2 Å s^{-1} and 6 nm BCP at a rate of 0.2 Å s^{-1} were thermally evaporated on the perovskite thin film sequentially (AE, Angstrom Engineering Inc) respectively, without breaking vacuum. Finally, 100 nm thick Ag electrode at a rate of 1.5 Å s^{-1} was deposited to complete the devices for current density-voltage (*J-V*) measurements or stability tests. For the fabrication of flexible devices, the flexible ITO-PET substrates were used and the other procedures were the same as the ones described

earlier. For the aging tests under mechanical stresses, the system employed was set up in the nitrogen glovebox using a uniaxial tester (PR-BDM-100, Puri, China).

Device Characterization

J-V characteristics of photovoltaic cells were taken using a Keithley 2400 source measure unit under a simulated AM 1.5G spectrum, with an Oriel 9600 solar simulator. The illumination light was calibrated to 100 mW cm^{-2} AM 1.5G using a silicon reference cell. Typically, the devices were measured in reverse scan (1.20 V→0 V, step 0.02 V). All the devices were measured without pre-conditioning such as light-soaking and applied a bias voltage. Steady-state power conversion efficiency was calculated by measuring stabilized photocurrent density under a constant bias voltage. External quantum efficiencies (EQEs) were measured using an integrated system (Enlitech Technology) and a lock-in amplifier with a current preamplifier under short-circuits' condition. Transient photocurrent decay (TPC) measurements under the short-circuit condition were conducted by photo-electrochemical measurement system.

Device stability tests

The stability test following the ISOS-L-2 protocol was conducted in the nitrogen atmosphere with continuous heating at ~65 ℃ and under continuous AM 1.5G illumination (100 mW cm^{-2}) at open-circuit condition for the unencapsulated devices. The PCEs of the devices were tracked over time and the *J-V* measurements were performed after cooling the devices down to room temperature. The maximum power point (MPP) tracking of the devices was conducted under AM 1.5G illumination (100 mW cm^{-2}) at ~50 ℃ and 85 ℃. The voltage at the MPP was automatically adjusted and applied, and the power output of the devices was tracked over time.

Materials Characterizations

Atomic force microscope (AFM) and its variants: For the AFM, conductive atomic force microscope (c-AFM) and Kelvin probe force microscope (KPFM) measurements of the 4PACz and SAX fresh films, the films were prepared on cleaned and dried ITO glass substrates in a nitrogen glove box by spin-coating the 4PACz and SAX solutions (0.002 mmol/mL in mixed solvent of methanol and DMF at volume ratio 2:1) at 1000 rpm for 10 s and subsequently 3000 rpm for 40 s, followed by annealing at 130 °C for 20 min. The samples were then transferred into a container filled with nitrogen after cooling down to the room temperature. The as-prepared samples were subsequently sent out for the AFM, c-AFM and KPFM measurements using the Jupiter XR Oxford Instruments. For all c-AFM measurements, a bias of 400 mV was applied.

Contact angle measurements: For the contact angle measurements, the 4PACz and SAX films were prepared using the same method as for the AFM measurements. The 4PACz or SAX film covered ITO glass substrates were recorded in a range of 0~180° with high precision (±0.1° accuracy) using a CA200 contact angle analyzer.

Photoelectron spectroscopy: For the high-resolution X-ray photoelectron spectroscopy (XPS) and ultraviolet photoelectron spectroscopy (UPS) measurements, the 4PACz and SAX films were prepared using the same method as for the AFM measurements as

mentioned previously. The samples were then into the XPS instrument (ThermoFisher ESCALAB Xi+) and an Al Kα (1486.6 eV) X-ray was used as the excitation source. The UPS measurements were carried out to determine the work function and the position of valence band maximum of materials. A He discharge lamp, emitting ultraviolet energy at 21.2 eV, was used for excitation. All UPS measurements were performed using standard procedures with a -10 V bias applied between the samples and detectors. Clean and etched gold was used as a reference.

Powder Raman: For the powder Raman spectroscopy, the 4PACz and SAX powder were stored in brown vials filled with nitrogen before sent out for measurements. The powder Raman was realized on Alpha300RAS (WITec GMBH, Germany) Raman system. A diode-pumped solid-state laser (532 nm, cobalt Laser) was focused on sample with a diffraction-limited beam size of 900 nm by a long working distance 50X Zeiss LD EC Epiplan-Neofluar Dic objective (NA=0.55). A G2 grating (600 g/mm, BLZ=500 nm) was used. To get a better spectral signal-to-noise ratio, the laser power was set to 1 mW, the integration time of collecting spectrum was set to 40 s, and the number of accumulations was set to be 9.

Fourier Transform infrared spectroscopy: For the FTIR measurements, 4PACz was dissolved in a mixed solvent of methanol and DMF at a volume ratio of 2:1. The solutions were deposited onto glass substrates and dried at 130 °C in a nitrogen glove box to remove the solvent before the measurements. The FTIR spectra was collected at room temperature by an FTIR spectrometer (ThermoFisher Nicolet iS50) equipped with a DTGS KBr detector. Spectral resolution was set to 1 cm^{-1}, aperture to 4 mm, and spectra were acquired by averaging 64 scans.

Polarized Raman spectroscopy: For the polarized Raman measurements, the 4PACz and SAX films were prepared by spin-coating the 4PACz and SAX solutions with a higher concentration of 0.03 mmol/mL in the mixed solvent indicated previously in order to make thicker films for better signals. Afterwards, the film was annealed at 130 °C for 20 min as fresh sample. The polarized Raman measurement was realized on Alpha300RAS (WITec GMBH, Germany) Raman system. A diode-pumped solid-state laser (633 nm, cobalt Laser) was focused on sample with a diffraction-limited beam size of 900 nm by a long working distance 50X Zeiss LD EC Epiplan-Neofluar Dic objective (NA=0.55). A G1 grating (300 g/mm, BLZ=500 nm) was used. To get a better spectral signal-to-noise ratio, the laser power was set to 15 mW and the integration time of collecting spectrum was set to 5 s, and the number of accumulations was set to be 20. An analyzer was inserted to polarize the incident laser beam. The angle of the analyzer was set to be 0°, 15°, 30°, and 45°, respectively. The polarization angle is twice the analyzer angle, which is 0°, 30°, 60°, and 90°, respectively.

Time-resolved photoluminescence (TRPL) spectroscopy: For TRPL measurement, the perovskite layers were prepared following the recipe indicated earlier. The sample was excited with a picosecond pulsed diode laser (Pico-quant LDH 450), with a ~70 ps pulse width and 20 MHz repetition rate, focused on sample with a 100x objective (NA = 0.90). The PL signal was acquired through the TCSPC strobelock system. The total instrument response function (IRF) for the PL decay was less than 200 ps, and the

temporal resolution was less than 30 ps. The energy density of laser for TRPL measurements was set to be 2.6 nJ/cm^2 and 26.2 nJ/cm^2 respectively.

X-Ray Diffractometer (XRD): For the assessment of perovskite films deposited on the top of the molecular layers, the perovskite layers were prepared following the recipe indicated previously. For the measurements of the molecular films, the films were prepared using the same method as for the polarized Raman spectroscopy measurements as mentioned earlier. XRD data were collected in reflection mode at room temperature on a D8 advance diffractometer equipped with a 1D LynxEye detector using monochromated Cu-Ka radiation.

Scanning electron microscope (SEM): The surface and cross-sectional morphologies of the perovskite films were carried out on the Field Emission Environment Scanning Electron Microscope of QuattroS. The preparation method for perovskite films is the same as mentioned earlier.

Ultra-performance liquid chromatography: We used the UPLC to semi-quantify the density of the molecules in the as-deposited films of 4PACz. The 4PACz films were prepared using the same method as for the AFM measurements as mentioned previously. We placed 17 substrates into a 20 mL brown vial and added 10 mL methanol. The molecules were removed from the ITO substrates by ultrasonic exfoliation and dissolved in menthol for the UPLC measurements. The density of the molecules on each substrate was determined by the total molecular concentration divided by the area of the substrate and the number of substrates used. Quantification analysis of 4PACz was carried out by ultra-performance liquid chromatography instrument (ACQUITY UPLC, H-Class, Waters) coupled with photodiode array detector (PDA) with BEH T3 column (1.8 um, 2.1*100 mm, Waters). The mobile phase A is water solution (0.1% formic acid, v/v) and mobile phase B is acetonitrile. The initial mobile phase is 30% B, increasing to 100% B in 2 min and maintaining for 2 min later. The post running time is 3.0 min. The elution is performed at 40 °C with flow rate of 0.4 mL/min. Single PDA channels at 330 nm was used for 4PACz. All data were collected and processed with Empower 3 software.

Ellipsometer: Ellipsometer (J.A. Woollam RC2 XI+) was used to measure the film thickness. We chose the Cauchy extended layer as the fitting model, where λ is the wavelength in μm, γ is the band edge energy in eV, $E(\lambda)$ is the energy of λ relative to the band edge in eV, $\eta(\lambda)$ determines whether the Cody Amplitude should be included, the *A*, *B*, *C* and *D* parameters always correspond to a wavelength in μm regardless of the spectral light units that CompleteEASE is configures to use. α is the Urbach amplitude, β is the Urbach exponent, and ρ is the Cody amplitude.

$$n(\lambda) = A + \frac{B}{\lambda^2} + \frac{C}{\lambda^4} + \frac{D}{\lambda^6} - IR \;\; \lambda^2$$

$$E(\lambda) = \frac{1.24}{\lambda} - \;\gamma$$

$$\eta(\lambda) = \begin{cases} 1, E(\lambda) > 0 \\ 0, E(\lambda) \leq 0 \end{cases}$$

$$k(\lambda) = \alpha \exp\big(\beta \;\; E(\lambda)\big) + \eta(\lambda) \;\; \rho \;\; E^2(\lambda)$$

Data availability:

All data are available in the main article and supplementary information, or on request from the corresponding authors. Source data are provided with this paper.

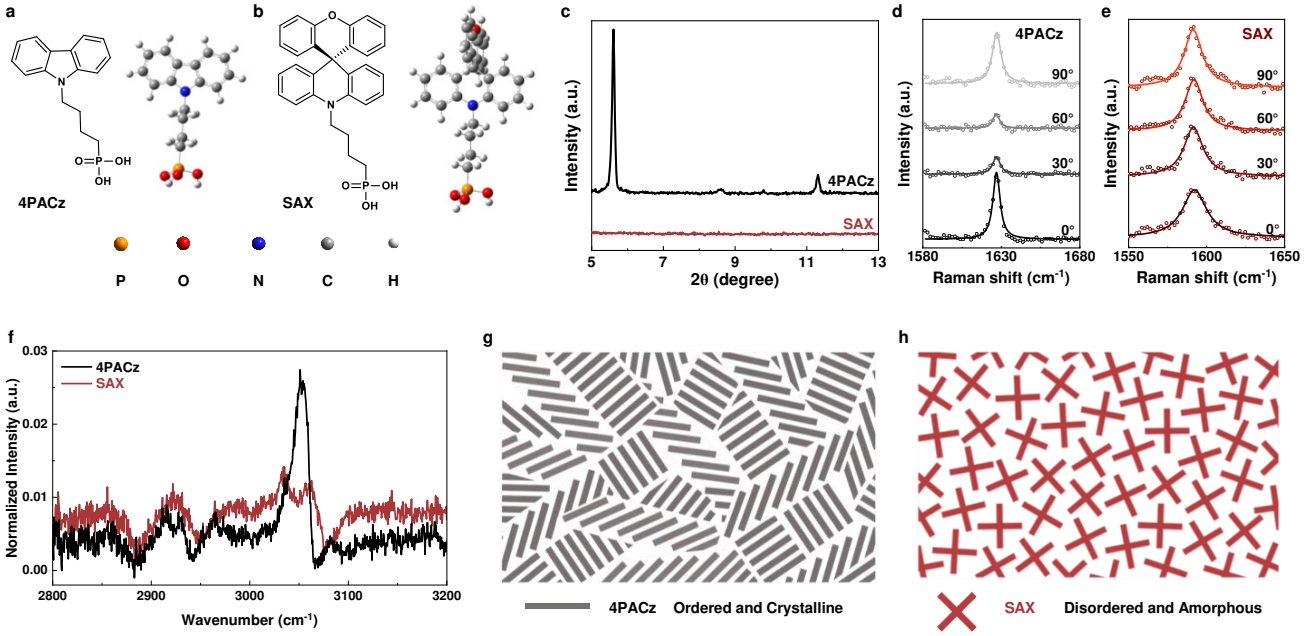
a
b
c
d
e
4PACz
SAX
P
O
N
C
H
Intensity (a.u.)
2θ (degree)
4PACz
SAX
90°
60°
30°
0°
Raman shift (cm-1)
f
Normalized Intensity (a.u.)
Wavenumber (cm-1)
g
4PACz Ordered and Crystalline
h
SAX Disordered and Amorphous

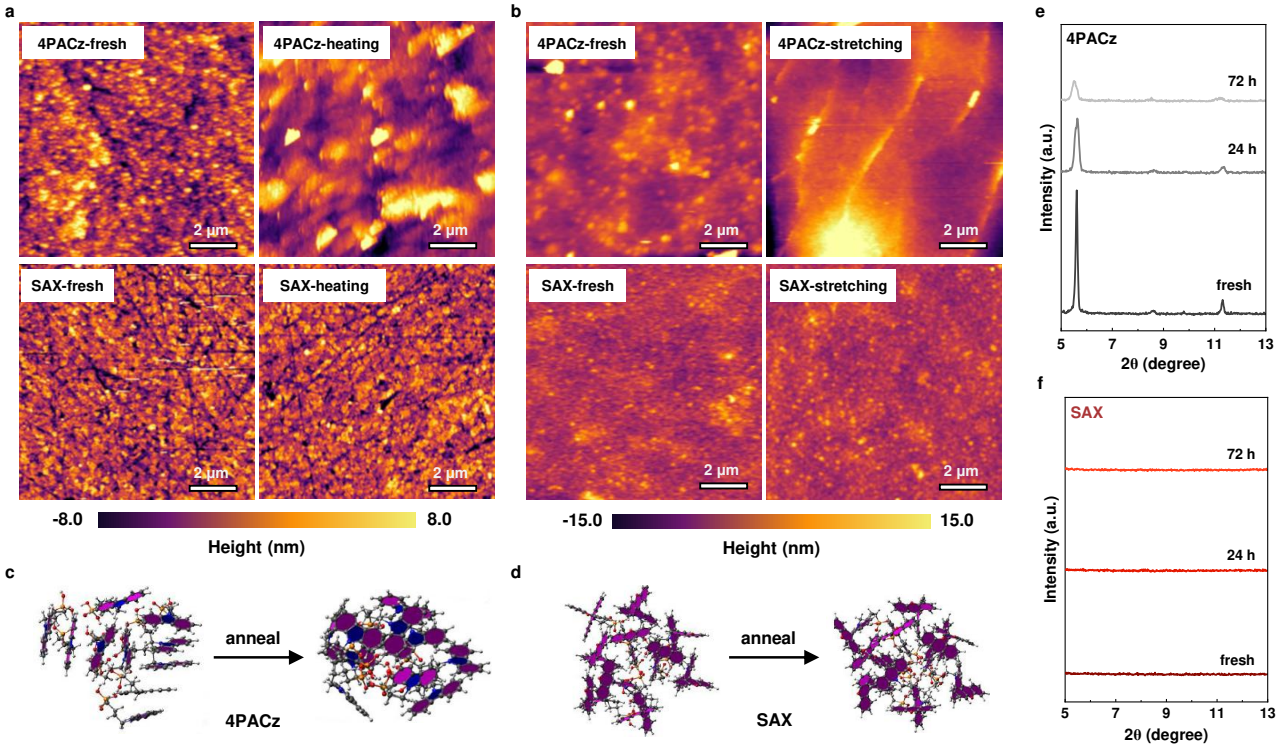
a
4PACz-fresh
4PACz-heating
2 μm
SAX-fresh
SAX-heating
-8.0
8.0
Height (nm)
b
4PACz-fresh
4PACz-stretching
SAX-fresh
SAX-stretching
-15.0
15.0
Height (nm)
c
anneal
4PACz
d
anneal
SAX
e
4PACz
72 h
24 h
fresh
Intensity (a.u.)
5
7
9
11
13
2θ (degree)
f
SAX
72 h
24 h
fresh
Intensity (a.u.)
2θ (degree)

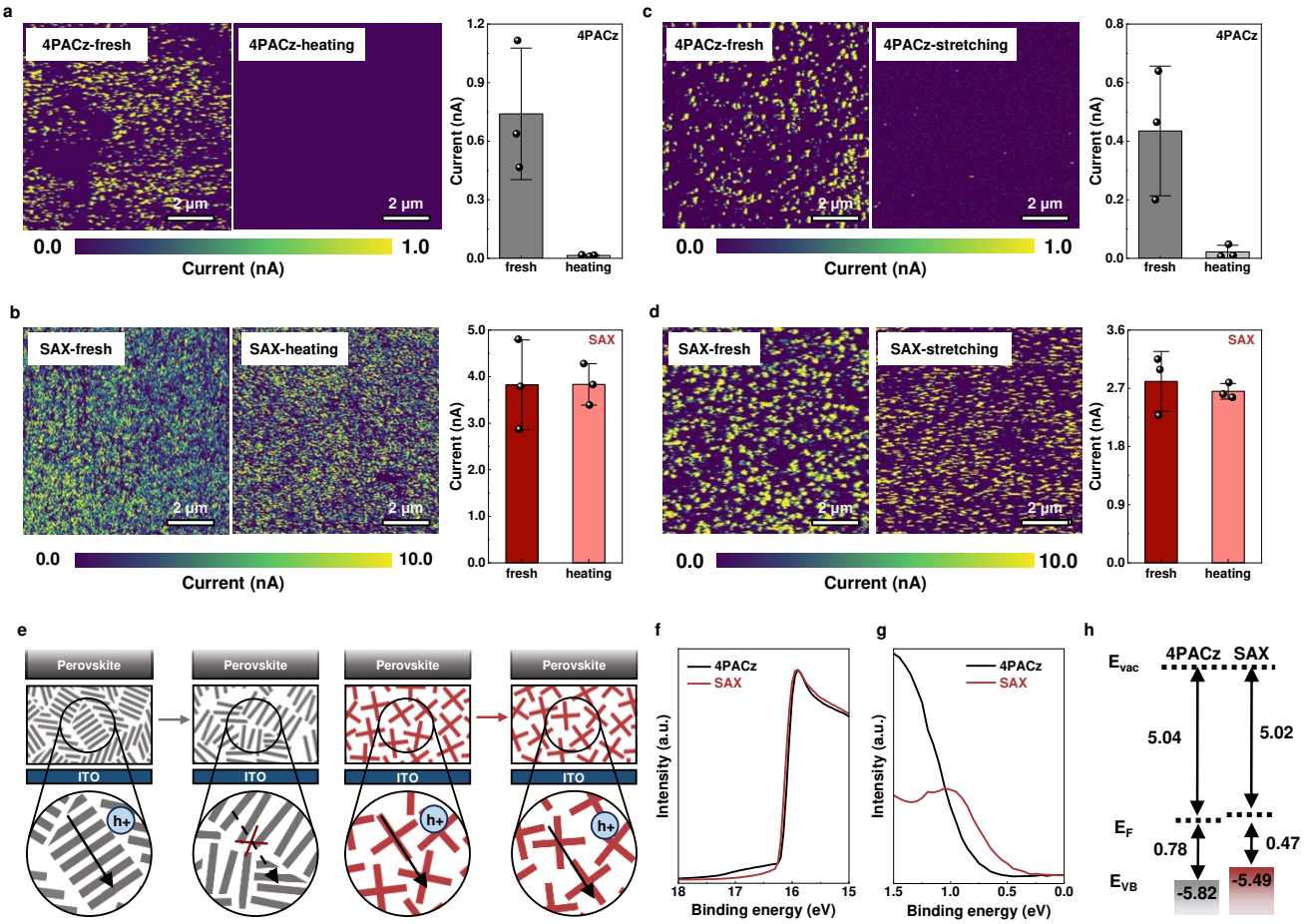
a
4PACz-fresh
4PACz-heating
2 μm
2 μm
0.0
1.0
Current (nA)
4PACz
Current (nA)
fresh
heating
c
4PACz-fresh
4PACz-stretching
2 μm
2 μm
0.0
1.0
Current (nA)
4PACz
Current (nA)
fresh
heating
b
SAX-fresh
SAX-heating
2 μm
2 μm
0.0
10.0
Current (nA)
SAX
Current (nA)
fresh
heating
d
SAX-fresh
SAX-stretching
2 μm
2 μm
0.0
10.0
Current (nA)
SAX
Current (nA)
fresh
heating
e
Perovskite
ITO
h+
f
4PACz
SAX
Intensity (a.u.)
Binding energy (eV)
g
4PACz
SAX
Intensity (a.u.)
Binding energy (eV)
h
4PACz
SAX
E_vac
5.04
5.02
E_F
0.78
0.47
E_VB
-5.82
-5.49

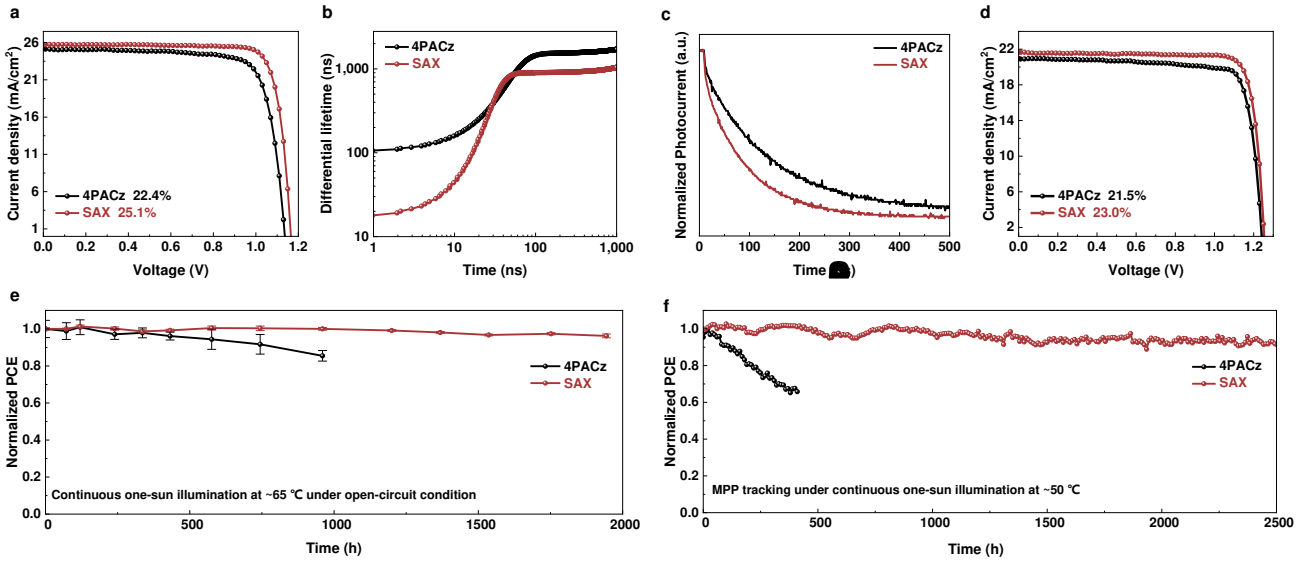
a
Current density (mA/cm²)
Voltage (V)
4PACz 22.4%
SAX 25.1%
b
Differential lifetime (ns)
Time (ns)
4PACz
SAX
c
Normalized Photocurrent (a.u.)
Time
4PACz
SAX
d
Current density (mA/cm²)
Voltage (V)
4PACz 21.5%
SAX 23.0%
e
Normalized PCE
Time (h)
4PACz
SAX
Continuous one-sun illumination at ~65 ℃ under open-circuit condition
f
Normalized PCE
Time (h)
4PACz
SAX
MPP tracking under continuous one-sun illumination at ~50 ℃

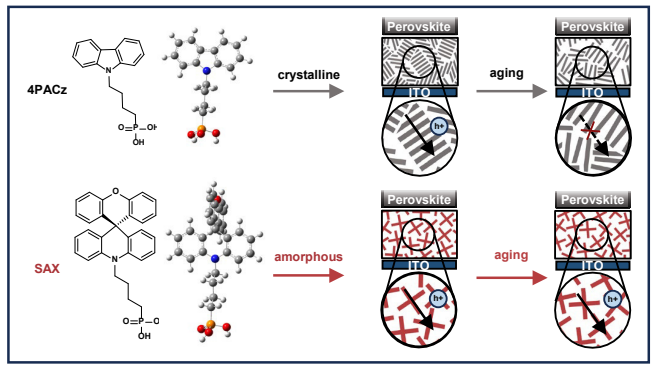
4PACz
crystalline
Perovskite
ITO
aging
Perovskite
ITO
SAX
amorphous
Perovskite
ITO
aging
Perovskite
ITO